J Mater Sci (2014) 49:3980–3995
DOI 10.1007/s10853-014-8038-1

Ab initio perspective of the ⟨110⟩ symmetrical tilt grain boundaries in bcc Fe: application of local energy and local stress

Somesh Kr. Bhattacharya · Shingo Tanaka · Yoshinori Shiihara · Masanori Kohyama

Received: 11 October 2013 / Accepted: 11 January 2014 / Published online: 5 February 2014

Abstract The mechanical properties of polycrystalline metals are strongly dependent on the microscopic structure, stability, and elastic properties of grain boundaries (GBs). By using ab initio local energy, local stress, and local Young's modulus, we attempt to provide a comprehensive view on the stability and structural properties of a series of ⟨110⟩ symmetrical tilt GBs (STGBs) in bcc Fe. We deal with four representative STGBs, the $\Sigma 3$ (112), $\Sigma 3$ (111), $\Sigma 11$ (332), and $\Sigma 9$ (221) GBs with the rotation angles ranging from 109.47° to 38.94°. The $\Sigma 3$ (112) GB shows special stability due to stable structural units of four-membered rings with negligible bond-length changes except for substantial bond-direction changes, like stacking faults or twins. The other GBs are constructed by periodic arrangement of 5–3 and bulk structural units as usual coincidence GBs, while the 5–3 unit in the $\Sigma 9$ (221) GB has an aspect of an edge-dislocation array in a small-angle tilt GB such as alternate compressive and tensile stresses at both the edges and relatively wide spread of local energy and local stress on both sides. In the GBs other than the $\Sigma 3$ (112) GB, there exist commonly two kinds of interface atoms; atoms with larger atomic volumes reveal higher local energies, tensile stresses, and enhanced magnetic moments, while the other kind of atoms forming compressed bonds reveal lower local energies, compressed stresses, and reduced magnetic moments. For the four GBs, the local Young's modulus averaged in the structural units ranges from 60 to 90 % of the bulk Young's modulus in accordance with the degree of structural disorder or GB energies. There exists clear correlation among the local Young's modulus, local energy, local stress, local magnetic moment, and local bonding nature at the structural units in the Fe GBs.

S. Kr. Bhattacharya (✉) · S. Tanaka · M. Kohyama
Research Institute for Ubiquitous Energy Devices, National Institute of Advanced Industrial Science and Technology, Midorigaoka, Ikeda, Osaka 563-8577, Japan
e-mail: somesh.bhattacharya@aist.go.jp

M. Kohyama
e-mail: m-kohyama@aist.go.jp

Y. Shiihara
Institute of Industrial Science, The University of Tokyo, Komaba, Meguro-ku, Tokyo 153-8505, Japan

Introduction

Iron and its alloys, owing to their high strength and toughness, play important roles in various industries, infrastructures, and our daily life as structural materials. The high strength and toughness of these polycrystalline materials are strongly affected by their grain boundaries, GBs [1, 2]. GBs act as barriers of dislocation transmission, and sources or sinks of dislocations or cracks. Therefore, detailed mechanical response of GBs including the behavior of dislocations or cracks at GBs has to be understood. For this purpose, we have to clarify the local elastic constants, cohesion (stability), and primary tensile or sliding behavior of GBs. The mechanical response of GBs should depend on two basic aspects: (a) the crystallographic viewpoint such as directions of rotation axes and interface planes, twist and tilt components, and rotation angles, and (b) the atomistic viewpoint of GB structures such as interfacial bonding, coincidence, periodicity or ordering, and presence of steps or dislocations. The picture of the structural units [3–6] can combine both the crystallographic and atomistic views, and the structural and mechanical properties of GBs can be effectively analyzed from the view point of the structural units.

Though limited information on GBs can be obtained from experiments, computer simulations provide an excellent alternative to gain an in-depth knowledge on the structural and mechanical properties of GBs at an atomistic level. For a series of ⟨110⟩ symmetrical tilt GBs (STGBs) with the [110] rotation axis in bcc Fe, Nakashima, and Takeuchi [7] proposed realistic models of GB structures in the whole range of the rotation angle, by classical molecular-dynamics (MD) simulations using empirical interatomic potentials. They obtained stable GB structures consisting of systematic arrangement and mixture of structural units, and obtained the curve of the GB energy versus the rotation angle. For STGBs, the structural units are composed of atomic rings in the projection along the rotation axis. Their results are consistent with the structural unit model, SUM [3–6] in accordance with previous examination of STGBs in other materials [8, 9]. Namely, an interface of a coincidence-site lattice (CSL) STGB with a specific rotation angle can be constructed by the periodic arrangement of structural units, and the kind and ratio of the structural units depend on the rotation angle. Special GBs, consisting of only one kind of structural units, correspond to the cusp in the curve of the GB energy versus the rotation angle, and a GB with a rotation angle between the two cusps can be constructed by a mixture of the structural units of the two special GBs at the cusps. For a lower rotation angle, a GB is formed by introducing one kind of structural units, corresponding to edge-dislocation cores, into the bulk crystal, which is consistent with the dislocation model of a small-angle tilt GB [10].

In the present study, we perform ab initio density functional theory (DFT) calculations of several ⟨110⟩ CSL STGBs in bcc Fe, following our preceding work on the $\Sigma 3$ (111) and $\Sigma 11$ (332) GBs [11], so as to grasp the perspective of the stability and structural properties of a series of ⟨110⟩ STGBs in bcc Fe. DFT calculations can provide comprehensive quantum mechanical description of the structural, mechanical, electronic, and magnetic properties of GBs [12], while the size of the supercells is limited compared to classical MD simulations. Such ab initio methods are essential in dealing with Fe GBs, because the electronic and magnetic structures play essential roles for the structural and mechanical properties of Fe GBs. Yesilleten et al. [13] argued that the stability of a Fe GB depends on the ferromagnetic nature of a GB. Using a tight-binding model, they pointed out the possibility that the exchange-energy gain by enhanced spin polarization at interface atoms could favor the GB stabilization. Our previous DFT calculations on the $\Sigma 3$ (111) and $\Sigma 11$ (332) GBs in bcc Fe [11], similar to the previous ab initio studies [14–16], clearly showed that the interface atoms in Fe GBs reveal large variations in magnetic moments, depending on local structural changes such as atomic volumes, interatomic distances, or coordination numbers. However, our calculations using the local energy and local stress analysis [17] indicated that the interface atoms forming covalent-like bonds with reduced magnetic moments contribute more to the stabilization than the interface atoms with enhanced magnetic moments. In any case, it is quite interesting to clarify the correlation among the local magnetic moment, local bonding, local stability, and local elastic or mechanical properties at Fe GBs.

In the present work, we deal with four kinds of ⟨110⟩ STGBs in bcc Fe, the $\Sigma 3$ (112), $\Sigma 3$ (111), $\Sigma 11$ (332), and $\Sigma 9$ (221) GBs with the rotation angles in the whole ranges as $\theta = 109.47°$, $70.53°$, $50.48°$, and $38.94°$, respectively. These four GBs can be regarded as representatives, consisting of typical arrangement of structural units as examined in [7]. The $\Sigma 3$ (112) GB consists of one kind of special structural units of four-membered rings, resulting in a very low GB energy, examined in a lot of simulations [7, 16, 18–20]. This GB has features as stacking faults or twins just like the $\Sigma 3$ (111) GB in fcc metals. The $\Sigma 3$ (111) and $\Sigma 11$ (332) GBs can be classified into typical CSL GBs consisting of ordered arrangement of usual structural units. As examined in our preceding work [11], the $\Sigma 3$ (111) GB consist of only the units of five-membered and three-membered rings (5–3 units), while the $\Sigma 11$ (332) GB consists of a mixture of the 5–3 unit and the bulk unit in the ratio of 1:1. The bulk unit constitutes the bulk crystal. Similar to usual CSL GBs, the $\Sigma 9$ (221) GB consists of a mixture of the 5–3 and bulk units in the ratio of 1:2 [7], while this GB seems to have an aspect of a small-angle tilt GB, because the 5–3 unit between the bulk units can be regarded as an edge-dislocation core introduced into the bulk crystal. In this way, the present examination of the four kinds of GBs should lead to the understanding of all the types of GBs as "stacking-fault type," "usual CSL GB type," and "small-angle GB type." Note that ⟨110⟩ STGBs occur more commonly in polycrystalline Fe compared to STGBs around other tilt axes, while previous ab initio studies of Fe GBs frequently dealt with ⟨001⟩ STGBs [14–16].

Following our preceding work [11], we apply the local energy and local stress scheme [17] to all the STGBs. This scheme can clarify the distributions of ab initio local energy and local stress inside the supercell by integrating the energy density and stress density in proper local regions satisfying the gauge-independent conditions with a robust numerical technique of the Bader integration [21]. We can investigate the stability and status of each atom or each structural unit in each GB via atomistic local energy and local stress as performed in [11, 22]. In this paper, we additionally obtain local Young's modulus of each atom in each GB by small tensile and compression tests coupled with the local strain via the Voronoi-volume analysis. This can clarify the direct effects of structural disorder or bond

weakening on the local elastic or mechanical responses of GBs. Within our knowledge, this kind of local Young's modulus analysis is being performed for the first time. By combining all these examinations, we can obtain the correlation among the local energy, local stress, local magnetic moment, local bonding nature, and local elastic property for each interface atom in the four kinds of ⟨110⟩ STGBs, which leads to the understanding of the underlying mechanism or principle for the stability as well as structural and mechanical properties of a series of ⟨110⟩ STGBs in bcc Fe.

Methodology

GB models

Figure 1 shows the supercell models of the four kinds of ⟨110⟩ STGBs. In each GB, there are two atomic planes in one period along the [110] direction (y direction) with the heights of $y = 0$ and $y = |\mathbf{b}|/2$ ($|\mathbf{b}| = \sqrt{2}a_0$). To illustrate the different atomic layers parallel to the interface, atomic layers are labeled by the numbers from the interface mirror plane in each GB. For the $\Sigma 3$ (112) GB, the 24-atom supercell is constructed by stacking 24 (112) atomic layers (one atom per layer) where one interface is introduced in every 12 layers. The translation vectors of the supercell are $4a_0[\bar{1}12]$, $a_0[110]$ and $\frac{1}{2}a_0[1\bar{1}1]$. The interface is constructed by a simple structural unit of a four-membered ring as examined in MD simulations [7, 18–20]. For the $\Sigma 3$ (111) GB, the 48-atom supercell is constructed by stacking 24 (111) atomic layers (two atoms per layer), where one interface is introduced in every 12 layers. The translation vectors are $4a_0[\bar{1}11]$, $a_0[110]$ and $a_0[1\bar{1}2]$. The interface consists of the 5–3 units as explained earlier. For the $\Sigma 11$ (332) GB, the 42-atom supercell is constructed by stacking 42 (332) atomic layers, where one interface is introduced for every 21 atomic layers. Each layer contains one atom, while the two atoms, "1a" and "1b", are moved and located on the interface plane after stacking the layers, so as to attain the mirror symmetry. The translation vectors are $\frac{21}{11}a_0[\bar{3}32]$, $a_0[110]$ and $\frac{1}{2}a_0[1\bar{1}3]$. The interface is constructed by a mixture of the 5–3 and bulk units with a ratio of 1:1. For the $\Sigma 9$ (221) GB, the 64-atom supercell is constructed by stacking 32 (221) atomic layers (two atoms per layer), where one interface is introduced per 16 atomic layers. After stacking the layers, six atoms as "1a", "1b", and "1c" are moved and located on the interface plane so as to satisfy the mirror-plane symmetry. The translation vectors are $2a_0[\bar{2}21]$, $a_0[110]$ and $a_0[1\bar{1}4]$. One period of the interface consists of two bulk and one 5–3 units. For the present four STGBs, all the interface models have the mirror-plane symmetry [7], and thus the rigid-body translation (RBT) is permitted only in the direction normal to the interface in each system. Thus, the translation vector normal to the interface contains twice the RBT in addition to that explained above.

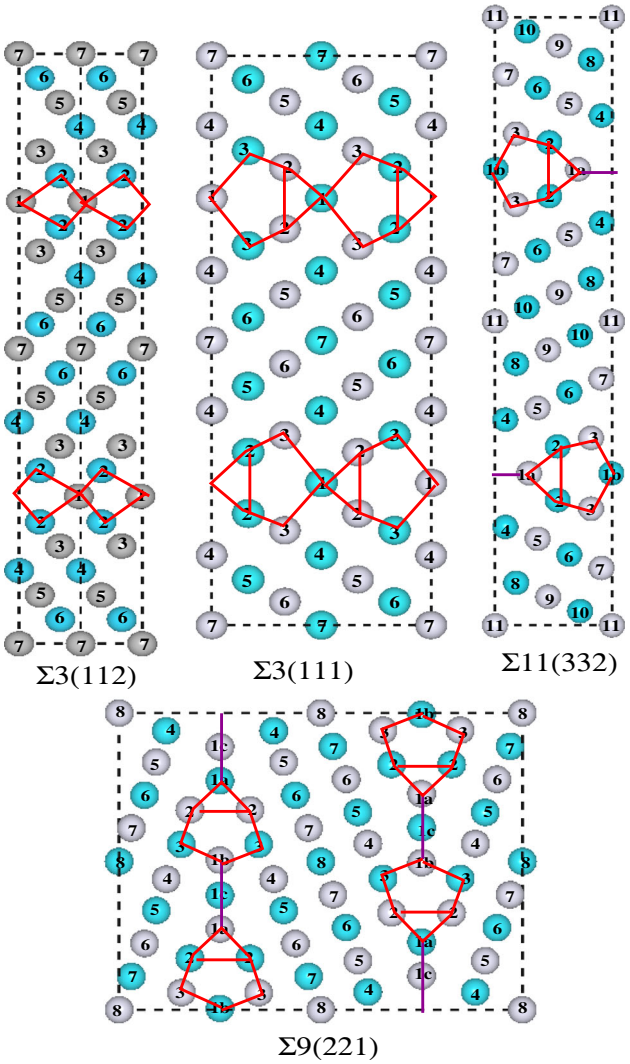

Fig. 1 (*Color online*) Optimized geometries of the four ⟨110⟩ STGBs in bcc Fe. The *gray* and *blue balls* depict the Fe atoms in the planes of $y = 0$ and $y = |\mathbf{b}|/2$ in each GB supercell. The *red solid lines* show the atomic rings of the structural units for each case. The *solid magenta line* indicates the bulk unit

PAW-GGA scheme

In our DFT calculations, the electron–ion interaction was described using the PAW method [23, 24], and the exchange-correlation energy was described by the spin-polarized generalized gradient approximation (GGA) with the Perdew–Burke–Ernzerhof functional [25]. We used a cutoff energy of 360 eV for the plane-wave basis and the

Brillouin zone integration was performed using the Monkhorst–Pack scheme [26]. We used **k**-point meshes of $2 \times 12 \times 20$, $4 \times 12 \times 8$, $2 \times 12 \times 10$, and $4 \times 12 \times 4$ for the supercells of the $\Sigma 3$ (112), $\Sigma 3$ (111), $\Sigma 11$ (332), and $\Sigma 9$ (221) GBs, respectively, to sample the Brillouin zone. We used Vienna Ab initio Simulation Package (VASP) [27, 28] for the structural relaxations, and Quantum Materials Simulator (QMAS) package for the energy density and stress density calculations [29]. In both the packages, the optimized lattice parameter is almost the same (2.83 Å), and the energy increases and atomic forces for relaxed configurations are also almost the same, because both the programs use the same PAW-GGA scheme with similar parameters. The atomic relaxation according to the Hellman–Feynman forces was performed using the quasi-Newton method. The convergence criteria for total energy and forces were set to 10^{-6} eV and 10^{-4} eV Å^{-1}, respectively. Further details are provided in [11].

The GB energy γ_{GB} is defined as

$$\gamma_{\mathrm{GB}} = \frac{E_{\mathrm{GB}} - E_{\mathrm{BC}}}{2A}, \tag{1}$$

where E_{GB} and E_{BC} are the total energies of the GB supercell and its corresponding bulk supercell. The latter was constructed so as to have similar periodicity to the GB supercell. The usage of common **k** points for E_{GB} and E_{BC} can greatly reduce numerical errors in Eq. (1). A is the area of the GB plane per one CSL period, and the factor of 2 comes from the presence of two interfaces in the GB supercell. The GB excess energy Δ and GB free volume Ω are defined as follows:

$$\Delta = \frac{E_{\mathrm{GB}} - E_{\mathrm{BC}}}{2}, \tag{2}$$

$$\Omega = \frac{V_{\mathrm{GB}} - V_{\mathrm{BC}}}{2A}, \tag{3}$$

where V_{GB} and V_{BC} are the volumes of the GB supercell and its corresponding bulk crystal with the same number of atoms.

Local energy and local stress

Following our preceding work [11], we apply the local energy and local stress scheme [17, 22] to Fe STGBs. The energy density $\varepsilon(\mathbf{r})$ and stress density $\tau_{\alpha\beta}(\mathbf{r})$ are defined as

$$E_{\mathrm{tot}} = \int_V \varepsilon(\mathbf{r})\mathrm{d}\mathbf{r}, \tag{4}$$

and

$$\sigma_{\alpha\beta} = \frac{1}{V}\frac{\partial E_{\mathrm{tot}}}{\partial \epsilon_{\alpha\beta}} = \frac{1}{V}\int_V \tau_{\alpha\beta}(\mathbf{r})\mathrm{d}\mathbf{r}, \tag{5}$$

where E_{tot} and $\sigma_{\alpha\beta}$ are the total energy and stress tensor, respectively, obtained by the conventional DFT scheme using the supercell (unit cell) with a volume of V. As explained in [17], the densities can be computed within the PAW-GGA framework as data on fast Fourier transformation mesh grids, by using the self-consistent charge density and wave functions of eigen states after obtaining the stable configuration. The local energy ε_i and local stress tensor $\sigma^i_{\alpha\beta}$ of an ith local region with a volume V_i in the supercell are given by the integration of the densities as

$$\varepsilon_i = \int_{V_i} \varepsilon(\mathbf{r})\mathrm{d}\mathbf{r}, \tag{6}$$

and

$$\sigma^i_{\alpha\beta} = \frac{1}{V_i}\int_{V_i} \tau_{\alpha\beta}(\mathbf{r})\mathrm{d}\mathbf{r}. \tag{7}$$

As discussed in [17, 30, 31], however, the local energy and local stress suffer from the gauge-dependent problem of the kinetic terms, namely the non-uniqueness for the selection of the symmetric and asymmetric forms of the kinetic terms in the energy and stress densities. For the local energy and the diagonal sum of the local stress tensor (hydrostatic pressure), the gauge-dependent problem can be settled if the energy and stress densities are integrated in a local region to satisfy the following condition:

$$\int_{V_i} \nabla^2\rho(\mathbf{r})\mathrm{d}\mathbf{r} = \int_{S_i} \nabla\rho(\mathbf{r}) \cdot \mathbf{n}_\perp \mathrm{d}S = 0, \tag{8}$$

where $\rho(\mathbf{r})$ is the valence electron density distribution. This is derived because the differences between the symmetric and asymmetric forms of the kinetic terms in the energy density and in the diagonal sum of the stress density are proportional to the term $\nabla^2\rho(\mathbf{r})$ [17]. The integration of this term throughout the supercell is naturally zero, while this term has to be integrated to be zero in the local region so as to remove the ambiguity in the local energy and local stress (diagonal sum).

It is not so easy to partition the supercell into local regions to satisfy Eq. (8) except for simple layered configurations such as surface slabs [17]. We adopt the Bader partitioning [32] to define atomic regions satisfying Eq. (8), and obtain the atomic energy and atomic stress (diagonal sum) via the integration of the energy and stress densities in such an atomic region. In Eq. (8), the volume integral for V_i is transformed into the surface integral on the region boundary S_i, which is equivalent to the condition of the Bader partitioning of the charge density. Namely, the gradient of the charge density along the normal direction of

the region boundary surface should be zero. Recently, a robust numerical algorithm for the Bader partitioning of uniform grid data was developed by Yu and Trinkle [21], which was successfully applied to the local energy calculation [33]. We apply this algorithm to the local energy and local stress in Fe GBs as successfully examined in [11, 22]. After calculating the atomic energy, the energy increase, $\Delta\varepsilon_i$, is obtained by subtracting the bulk energy per atom, which is obtained by the bulk supercell mentioned above. About the atomic stress, we obtain the diagonal sum as $\sigma^i = \sum_\alpha \sigma^i_{\alpha\alpha}$.

There is also the gauge-dependent problem about the electrostatic terms in the energy and stress densities, in addition to the kinetic terms. According to our preceding studies [11, 17, 22], we adopt the Maxwell form, similar to the original formulations of the energy and stress densities [30, 31]. There have been discussions about the selection of the Maxwell and Coulomb forms in the electrostatic energy density [33], and the selection of the Maxwell and Kugler forms in the electrostatic stress density [34–36]. As adopted in [33], it may be possible to define two kinds of local regions to satisfy the gauge-independent conditions for the kinetic and electrostatic terms, respectively, while this is not adopted in the present work, according to the previous arguments to support the superiority of the Maxwell form [34, 37].

Local Young's modulus

In order to investigate the elastic property of each GB, first, we calculate a cell-averaged Young's modulus in the direction normal to the interface via small tensile and compressive deformations of the stable GB supercell. In the linear regime of small strains, we can obtain the cell-averaged Young's modulus as follows:

$$Y_{\mathrm{GB}} = \frac{T(+\delta) - T(-\delta)}{2\delta}, \tag{9}$$

where $T(-\delta)$ and $T(+\delta)$ are the compressive and tensile stresses, respectively, under the small compression and tension of δ in the direction normal to the interface of the GB supercell, as σ_{xx} in the present supercell. Here we ignore the Poisson ratio. Namely, the compressive and tensile deformations are introduced with the fixed cell dimensions parallel to the interface. The stresses are obtained by the conventional cell-averaged scheme [34] after enough relaxation of inner coordinates. We adopt $\delta = 0.02$ (2 %).

Of course, Y_{GB} in Eq. (9) contains the effects of the bulk regions in the supercell, and depends on the ratio of the bulk regions. It is desirable to obtain the local Young's modulus at the interface region. If we obtain the relation between the local stress and local strain at the interface region in the supercell under the small compression and tension of δ, we could evaluate the local Young's modulus as the gradient of the local stress with respect to the local strain. The present local stress scheme itself cannot be used for this purpose, because only the diagonal sum is free from the gauge-dependency in the present scheme, except for special configurations such as surface slabs [17]. Thus, we adopt the cell-averaged stress T as the local stress coupled with the local strain defined by some proper method. We evaluate the local strain by atomic-volume changes obtained by the fuzzy-Voronoi scheme [38]. Then, an atomic local Young's modulus is obtained as follows:

$$Y_i = \frac{T(+\delta) - T(-\delta)}{V_i(+\delta)/V_i^0 - V_i(-\delta)/V_i^0}, \tag{10}$$

where $V_i(+\delta)$ and $V_i(-\delta)$ are the Voronoi volumes of an ith atom in the GB supercell under the small tension and compression of δ. V_i^0 is the atomic volume in the GB supercell without any strain, namely in the most stable configuration. In the present local Young's modulus, the effect of local structure is included only via the local strain as V_i/V_i^0. There may exist other methods to define local strains, while the present scheme is suitable to the present deformation calculations without changes of cell dimensions parallel to the interface and can include the effects of local structural changes naturally.

Results

GB energies and stable configurations

We summarize our DFT results of the GB energy, excess energy, and excess volume in Table 1. The GB energy increases in the order of the Σ3 (112), Σ11 (332), Σ3 (111), and Σ9 (221) GBs. The Σ3 (112) GB is very stable, while the Σ9 (221) GB has the largest GB energy. The Σ11 (332) GB is slightly more stable than the Σ3 (111) GB as examined in our preceding work [11]. The present tendency of the relative stability among the four GBs is rather similar to the trend observed by Nakashima and Takeuchi

Table 1 Calculated GB energy γ_{GB}, GB excess energy Δ, and GB excess volume Ω for the four ⟨110⟩ STGBs in bcc Fe

GB	θ (°)	γ_{GB} (J m^{-2})	γ_{GB}[a] (J m^{-2})	Δ (eV)	Ω (Å)
Σ3 (112)	109.47	0.43	0.3	0.266	0.10
Σ3 (111)	70.53	1.61	1.2	2.82	0.31
Σ11 (332)	50.48	1.49	0.9	1.78	0.22
Σ9 (221)	38.94	1.71	1.4	5.12	0.26

[a] Results by an empirical interatomic potential [7]

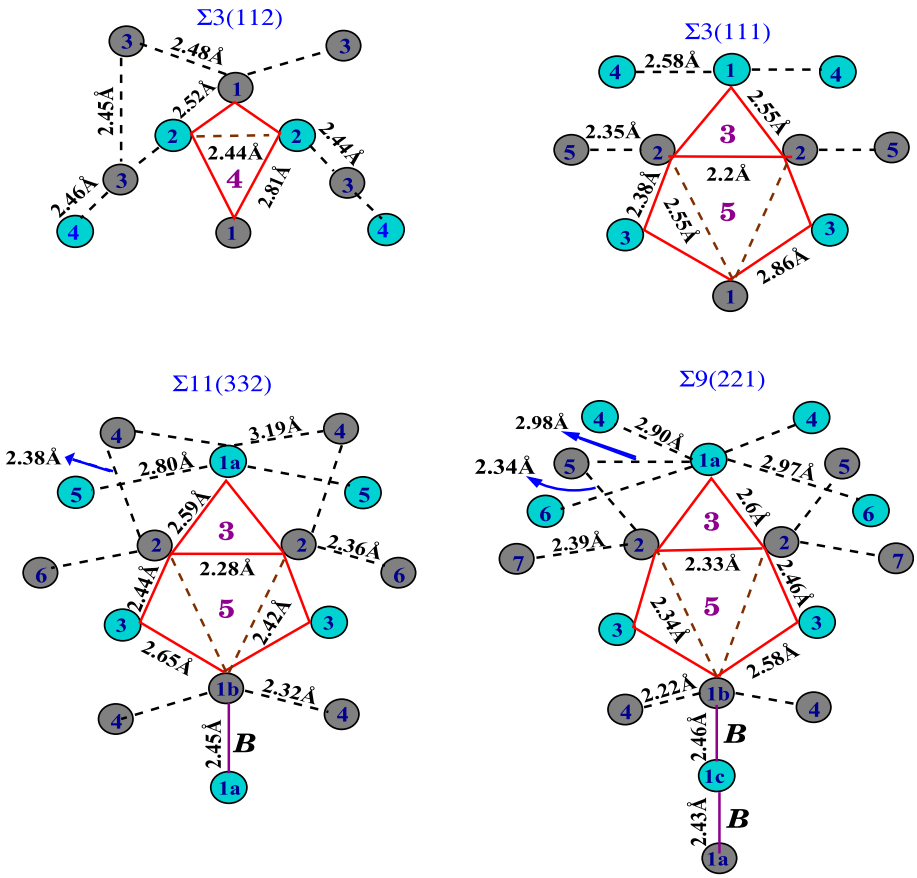

Fig. 2 (*Color online*) Schematic representations of the structural units and neighboring atoms of the four ⟨110⟩ STGBs in Fe. Bond lengths at and around the structural units in one CSL period of each relaxed configuration are shown. The two different atomic *colors* represent the two [110] planes in each GB supercell. The atomic *rings* constituting the structural units are indicated by *solid lines* and *numbers* in *magenta color*. The bulk units (*magenta lines*) in the $\Sigma 11$ (332) and $\Sigma 9$ (221) GBs are marked as ***B***

[7]. The values of γ_{GB} for the $\Sigma 3$ GBs are similar to other DFT results as 0.47 J m^{-2} [16] and 0.34 J m^{-2} [39] for the $\Sigma 3$ (112) GB, and 1.52 J m^{-2} [39] and 1.57 J m^{-2} [15] for the $\Sigma 3$ (111) GB.

The structural units of these GBs are shown in Fig. 2 with bond lengths in the relaxed configurations. Note that the bulk bond length is 2.45 Å, and that the bulk atom has four first neighbors on different (110) layers and the four first neighbors on the same (110) plane in the [110] projection. For the $\Sigma 3$ (112) GB in Fig. 2, the structural unit is a simple four-membered ring formed by atoms on layers "1" and "2". In this structure, all the atoms have eight first neighbors similar to the bulk crystal. For the atom on layer "1", the four first neighbors on different (110) planes are the atoms on layer "2" on both sides, and the four first neighbors on the same (110) plane are the atoms on layer "1" and the atoms on layer "3". There are slight interlayer dilatations between layers "1" and "2" and between layers "1" and "3", and thus the bond lengths around the atoms on layer "1" are slightly stretched. On the other hand, the bond directions from the atom on layer "1" to the atoms on layer "2" as the four first neighbors on the different (110) planes are quite different from the bulk structure. For the atom on layer "2", the four first neighbors on different (110) planes are the two atoms on layer "1" and the two atoms on layer "3". The other four first neighbors on the same (110) plane are the two atoms on the same layer "2", one atom on the other layer "2" across the interface, and the atom on layer "4". The atom on layer "2" has rather small bond-length and bond-angle distortions. For the atoms away from the interface after layer "2", bulk-like environment is almost recovered at least within the second neighbors. In this way, except for small bond stretching around the atom on layer "1", the remarkable structural disorder in this GB is only the bond-direction changes at the atoms on layer "1". This is the origin of the relatively smaller GB energy of this interface, as well as smaller variations in the magnetic moments and LDOSs (local density of states) features as explained later.

As shown in Fig. 2, the $\Sigma 3$ (111) GB is constructed only by the 5–3 units, while the ratio of the bulk units are increased in the order of the $\Sigma 11$ (332) and $\Sigma 9$ (221) GBs. The GB energy decreases from the $\Sigma 3$ (111) GB to the $\Sigma 11$ (332) GB by introducing the bulk unit, while the GB

energy increases from the Σ11 (332) GB to the Σ9 (221) GB with a higher ratio of the bulk units. In these three GBs, we can see considerable bond-length deviations from the bulk bond length (2.45 Å) as well as the changes in bond angles and coordination numbers at the interface. As shown in Fig. 2, the bond network at and around the 5–3 units is rather similar in the three GBs, while the bond lengths are substantially varied in each GB. There are several intriguing trends on the structural variations among these three GBs. First, the bond-length and bond-angle deviations are highly remarkable in the Σ9 (221) GB among the three GBs, which is related to the largest GB energy. Second, the atom on layer "1" or "1a" at the apex of the triangle of the 5–3 unit is commonly located in the tensile atmosphere with elongated bonds in the three GBs. The bond lengths around this atom are increased in the order of the Σ3 (111) GB, the Σ11 (332) GB, and the Σ9 (221) GB. For the atom on layer "1" in the Σ3 (111) GB, the bond length ranges from 2.55 to 2.86 Å. For the atom of "1a" in the Σ9 (221) GB, the bond length ranges from 2.6 to 2.97 Å, except for the compressed bonds (2.43 Å) between the atoms of "1a" and "1c". Third, in these GBs, the atom of "1b" at the apex of the other edge of the 5–3 unit has more compressed bonds around it from the Σ11 (332) GB to the Σ9 (221) GB. The bond length between the atom "1b" and the atoms on layer "4" is 2.22 Å in the Σ9 (221) GB, in contrast to the length of 2.32 Å for the corresponding bonds in the Σ11 (332) GB. Fourth, for the atom on layer "2" in the structural units, bond lengths around it are greatly compressed in the Σ3 (111) GB, which is gradually relaxed toward the Σ9 (221) GB via the Σ11 (332) GB. The bond length around the atom of layer "2" within 5–3 units ranges from 2.20 to 2.55 Å in the Σ3 (111) GB, from 2.28 to 2.59 Å in the Σ11 (332) GB, and from 2.33 to 2.6 Å in the Σ9 (221) GB. Fifth, there is a tendency that the bond distortions extend more widely in the order of the Σ3 (111) GB, the Σ11 (332) GB, and the Σ9 (221) GB. For example, the bond lengths around the atom on layer "4" with bulk-like eight neighbors range from 2.46 to 2.58 Å in the Σ3 (111) GB, from 2.32 to 2.50 Å in the Σ11 (332) GB, and from 2.22 to 2.90 Å in the Σ9 (221) GB. Similarly, bulk-like bonds around the atom on layer "5" range from 2.35 to 2.47 Å in the Σ3 (111) GB, from 2.45 to 2.83 Å in the Σ11 (332) GB, and from 2.34 to 2.54 Å in the Σ9 (221) GB.

Local energy and local stress

In order to understand the stability of the present GBs, the local energy and local stress are quite effective as shown recently [11, 22]. It is interesting to examine the stability of the structural units and the relation between the local structural disorder and the local energy and local stress.

Figure 3 shows the energy increase $\Delta\varepsilon_i$ for each atom in the GB supercell for the four STGBs. Figure 4 shows the two-dimensional plot of $\Delta\varepsilon_i$ on each (110) plane for the Σ3 (112) and Σ9 (221) GBs. Similar figures for the other two GBs are given in [11]. The value of $\Delta\varepsilon_i$ is very small in the bulk-like region in each GB supercell, validating the present scheme as well as the supercell size, while the bulk-like region in the supercell of the Σ9 (221) GB is rather narrow. The sum of $\Delta\varepsilon_i$ for all the atoms in the supercell is listed in Table 2, which is nearly twice the value of Δ in Table 1. Table 2 also lists the sums of $\Delta\varepsilon_i$ for the structural units or slightly wider regions at the interface, and the ratio ζ of the energy increase at the structural units against the total sum. As shown by the larger values of ζ in Table 2, the concentration of the energy increase at the interface is remarkable in the Σ3 (112) and Σ3 (111) GBs, consisting of only one kind of the structural units, which is consistent with the view of the SUM. The extent of the energy increase is a little wider in the Σ11 (332) GB and much wider in the Σ9 (221) GB as seen in Table 2 and Figs. 3 and 4. This tendency is correlated with the extent of the bond length and bond angle deviations in each GB as explained above. For the Σ3 (112) GB, the energy increase of the structural unit itself is rather small (0.21 eV as listed in Table 2) and the energy concentration is remarkable (over 99 % if the energy of the atoms on layer "3" is included), leading to the very small GB energy. The energy increase per one 5–3 unit (per six atoms) is 1.70, 1.41, and 1.52 eV for the Σ3 (111) GB, the Σ11 (332) GB, and the Σ9 (221) GB, respectively. Thus, the Σ11 (332) GB is more stable than the Σ3 (111) GB due to more stable 5–3 units, while the extent of the energy increase is a little wider as shown in Fig. 3. The introduction of the bulk unit seems to stabilize the 5–3 unit in the Σ11 (332) GB. Table 3 lists the energy increase of each interface atom. The atoms of "1a" and "1b" at the both edges of the 5–3 unit in the Σ11 (332) GB correspond to the atoms on layer "1" in the Σ3 (111) GB. The energy at the atom of "1b" in the Σ11 (332) GB is greatly stabilized, while the energy at the atom of "1a" is a little increased compared to the atom on layer "1" in the Σ3 (111) GB. For the Σ9 (221) GB, the energy at the atom of "1a" is greatly increased, and thus the energy of the 5–3 unit is increased, which is related to the increased bond stretching around the atom "1a" as mentioned above. In addition, the extent of the energy increase is much wider in the Σ9 GB, as clearly shown by the values of the atoms in layers "4" and "5" in Table 3 as well as in Figs. 3 and 4, leading to the very large GB energy.

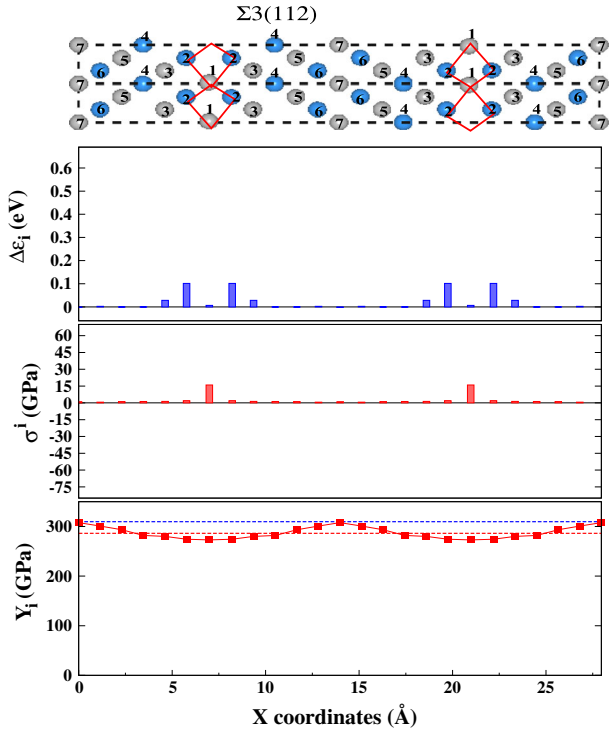
Σ3(112)
Δε_i (eV)
σ^i (GPa)
Y_i (GPa)
X coordinates (Å)

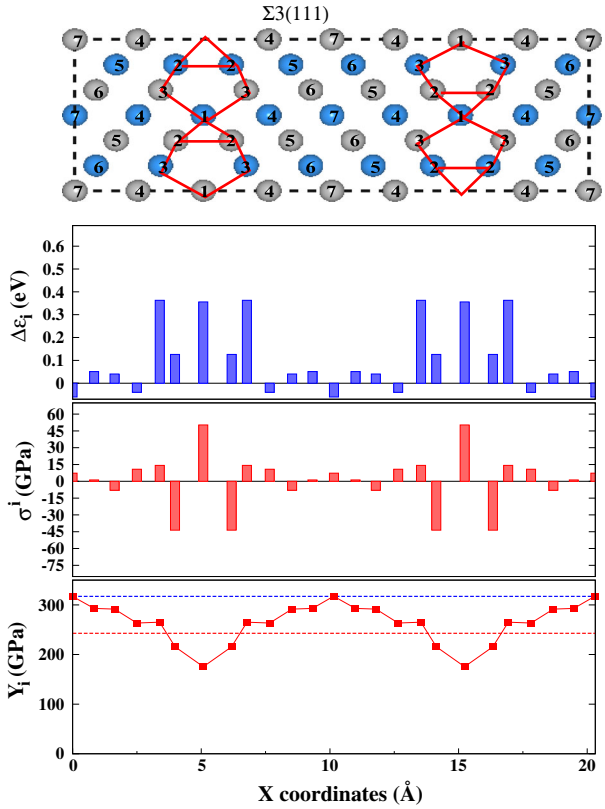
Σ3(111)
Δε_i (eV)
σ^i (GPa)
Y_i (GPa)
X coordinates (Å)

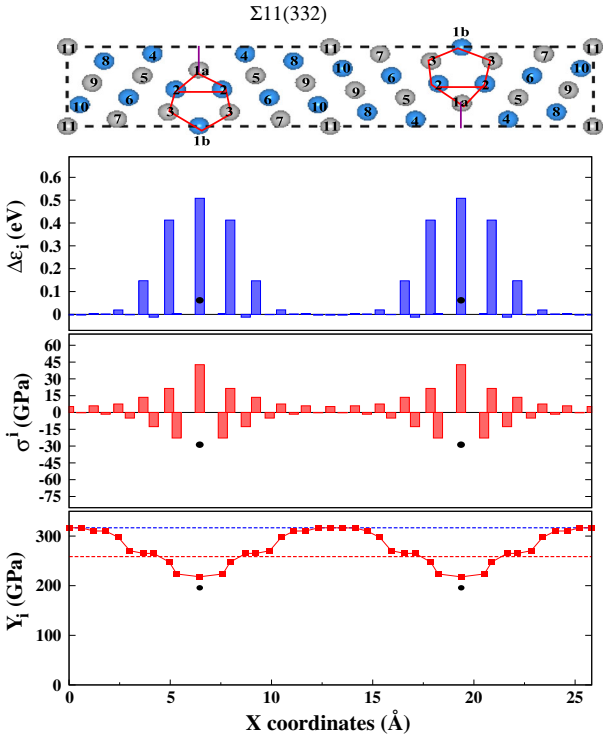
Σ11(332)
1a
1b
Δε_i (eV)
σ^i (GPa)
Y_i (GPa)
X coordinates (Å)

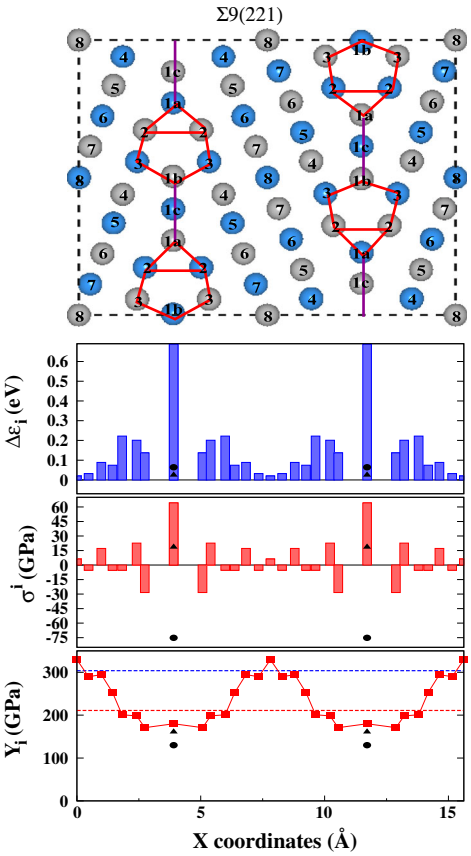
Σ9(221)
1a
1b
1c
Δε_i (eV)
σ^i (GPa)
Y_i (GPa)
X coordinates (Å)

◀**Fig. 3** (*Color online*) Atomic energy increase $\Delta\varepsilon_i$, atomic local stress (*diagonal* sum) σ^i and atomic Young's modulus Y_i of all the atoms in each GB supercell, compared to the atomic configuration, for the four GBs in Fe. The *filled circles* show the data for the atom "1b" in the Σ11 (332) and Σ9 (221) GBs, while *filled triangles* represent the data for the atom "1c" in the Σ9 (221) GB. *Red* and *blue horizontal broken lines* in each panel of atomic Young's moduli indicate the cell-averaged Young's moduli of the GB and bulk supercells, respectively, obtained by Eq. (9)

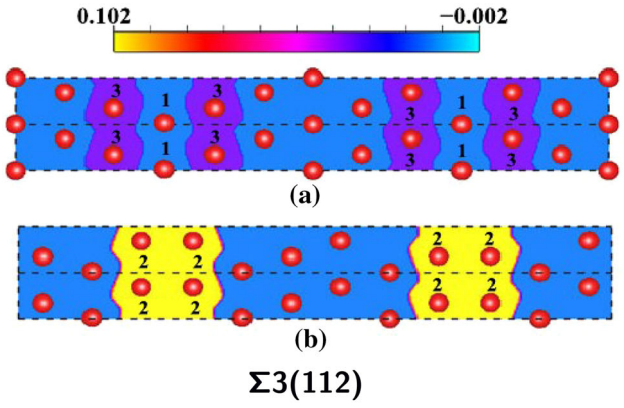

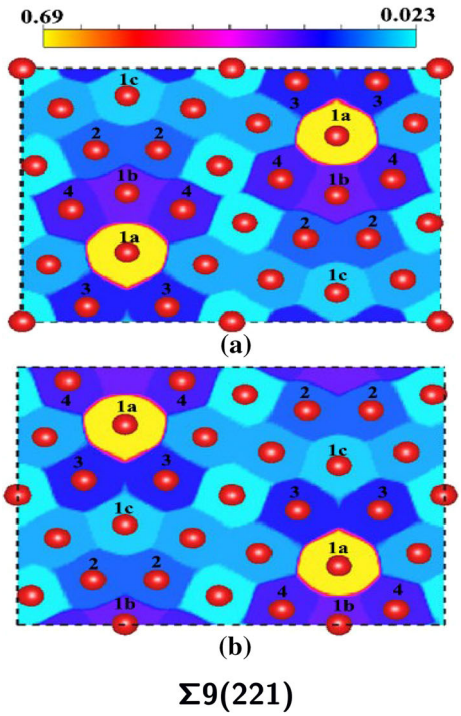

Fig. 4 (*Color online*) Plots of $\Delta\varepsilon_i$ (in eV) for the Σ3 (112) and Σ9 (221) GBs in Fe on the two (110) atomic planes of **a** $y = 0$ and **b** $y = |\mathbf{b}|/2$. *Different colors* represent different values of $\Delta\varepsilon_i$ of each Bader region

Figure 3 and Table 3 show the atomic stress (diagonal sum) for each atom in the GB supercell. Figure 5 shows the two-dimensional plot of the atomic stress on each (110) plane for the Σ3 (112) and Σ9 (221) GBs, while similar figures for the other two GBs are given in [11]. Here, the positive and negative stress values mean tensile and compressive stresses, respectively. Similar to the local energy, the stress values are very small in the bulk-like regions in the GB supercells, justifying the present local stress scheme and the supercell size, while the bulk region in the supercell of the Σ9 (221) GB seems to be a little narrow. The features of the local stresses at the interface regions show correlation with the local structural disorder. The Σ3 (112) GB with only the bond-direction disorder and small dilatation at the interface reveals small tensile stress only at the interface layer. In the other three GBs, the tensile and compressive stresses are generated due to the local environment. As analyzed in [11], there exist two kinds of atoms in the Σ3 (111) and Σ11 (332) GBs. One is an interface atom with a larger atomic volume or stretched bonds, revealing higher local energy and tensile stress, such as the atoms on layers "1" ("1a") and "3". The other is an interface atom forming shortened strong bonds with covalent character, revealing relatively lower energy and compressed stress, such as the atoms on layers "1b", "2", or "4". These features are also observed in the Σ9 (221) GB, where the atoms on layers "1a" and "3" seem to belong to the former and the atoms on layers "1b", "2", and "4" seem to belong to the latter. As shown in Figs. 3 and 5, the extent of the local stress distribution becomes wider in the order of the Σ3 (111), Σ11 (332), and Σ9 (221) GBs, similar to the local energy distribution.

Table 2 Sums of local energies $\Delta\varepsilon_i$ in interface regions in each GB supercell for the four GBs in Fe

GB	2 × Δ (eV)	Total sum supercell (eV)	Layers "1 - 3" (eV)	Layers "1 - 5" (eV)	ζ (%)
Σ3 (112)	0.532	0.5315	0.530 (0.418)	–	99.72 (78.65)
Σ3 (111)	5.64	5.62	5.36	5.36	95.37
Σ11 (332)	3.56	3.55	2.82	3.38	79.44
Σ9 (221)	10.24	10.19	6.2	8.52	60.84

Two kinds of interface regions from the interface layer to layer "3" and to layer "5" are dealt with. The former corresponds to the sum for the atoms in the structural units, except for the Σ3 (112) GB. In the Σ3 (112) GB, the sum from the interface to layer "2" corresponds to the sum for the structural unit as listed in the parentheses. The sum for all the atoms in the GB supercell is also compared to twice the GB excess energy Δ. ζ indicates the ratio of the sum for the structural units against the total sum

Table 3 Values of the local energy increase and the local stress (diagonal sum) for the interface atoms in the four GBs in Fe

GB	$\Delta\varepsilon_i$ (eV)							$\sum_\alpha \sigma^i_{\alpha\alpha}$ (GPa)						
Σ3 (112)	1	2	3	4				1	2	3	4			
	0.007	0.102	0.028	−0.002				15.94	1.81	1.31	1.26			
Σ3 (111)	1	2	3	4	5			1	2	3	4	5		
	0.36	0.13	0.36	−0.04	0.04			50.30	−43.62	14.24	10.78	−7.96		
Σ11 (332)	1a	1b	2	3	4	5		1a	1b	2	3	4	5	
	0.51	0.06	0.01	0.41	−0.01	0.15		42.64	−28.70	−22.76	21.49	−12.63	13.51	
Σ9 (221)	1a	1b	1c	2	3	4	5	1a	1b	1c	2	3	4	5
	0.69	0.07	0.03	0.14	0.20	0.22	0.07	64.17	−75.15	18.56	−28.39	22.64	−5.37	−5.52

From Figs. 2, 3, 4, and 5, and Table 3, we can obtain the information about the relation between the local energy and local stress and the local atomic structure in each GB.

For the Σ3 (112) GB, $\Delta\varepsilon_i$ is the highest in the atoms of layer "2", while the value of $\Delta\varepsilon_i$ is rather small. $\Delta\varepsilon_i$ of the atom on layer "1" is very small in spite of the remarkable bond-direction disorder at this atom, while $\Delta\varepsilon_i$ on layer "3" is a little larger than that on layer "1". About the atomic stress, there exists tensile stress at the atom of layer "1", which seems to be related to the largest volume increase at this atom in this GB (see Fig. 6). Although the stress normal to the interface should be relaxed, the residual stress components parallel to interface may exist associated with the different bond directions and small dilatation around the atom on layer "1".

For the other three STGBs, the bond network at the 5–3 unit is similar, while the local bond lengths are varied depending on the rotation angle and the ratio of bulk units introduced. As explained above, the atom of "1" or "1a" as the apex of the triangle of the 5–3 unit has stretched bonds around it, and reveals almost the highest energy increase and the highest tensile stress in each GB. The degree of the bond stretching around it becomes larger in the order of the Σ3 (111), Σ11 (332), and Σ9 (221) GBs. Thus, the value of $\Delta\varepsilon_i$ at the atom of "1" or "1a" becomes larger in the order of the Σ3 (111), Σ11 (332), and Σ9 (221) GBs as listed in Table 3. The tensile stress at this atom becomes a little lower from the Σ3 (111) GB to the Σ11 (332) GB due to the relaxation by the introduction of the bulk unit, while the stress at this atom becomes quite higher in the Σ9 (221) GB as listed in Table 3.

About the atom of "1b" as the other edge of the 5–3 unit in the Σ11 (332) and Σ9 (221) GBs, the bonds around it become more compressive from the Σ11 (332) GB to the Σ9 (221) GB as depicted in Fig. 2, thereby enhancing the magnitude of the compressive stress at this atom in the Σ9 (221) GB as listed in Table 3. This should be mainly caused by very short bonds (2.20 Å) between the atom "1b" and the atoms on layer "4". About the atom on layer "2" in these three GBs, the compression of bonds around it becomes relaxed in the order of the Σ3 (111), Σ11 (332), and Σ9 (221) GBs as shown in Fig. 2. Thus, the compressed stress is relaxed from the Σ3 (111) GB to the Σ11 (332) GB, while it increases a little from the Σ11 (332) GB to the Σ9 (221) GB, as listed in Table 3. The value of $\Delta\varepsilon_i$ at the atom on layer "2" also reveals similar behavior for these three GBs.

For the atoms on layers "3", "4", and "5" in the three GBs, it is clear that the extent of the energy increase and stress variation becomes wider in the order of the Σ3 (111), Σ11 (332), and Σ9 (221) GBs, in accordance with the extent of the bond-length and bond-angle deviations. In Table 3, the sum of $\Delta\varepsilon_i$ for the atoms on layers "4" and "5" is increased in this order. The magnitudes of the atomic stresses on layers "4" and "5" are increased from the Σ3 (111) GB to the Σ11 (332) GB. For the Σ9 (221) GB, the stress magnitudes on layers "4" and "5" are decreased, while the atomic stress on layer "6" is rather large.

In the Σ9 (221) GB, the atom of "1c" between the atoms of "1a" and "1b" reveals relatively low energy increase and low stress values. This is because this atom is located in the environment similar to the bulk crystal as the middle point of the two neighboring bulk units. In this GB, we can regard the 5–3 unit as a dislocation core arranged linearly in the bulk crystal by the following three aspects. First, the atoms at "1a" and "1b" as the both edges of the 5–3 unit reveal opposite tensile and compressive stresses, respectively, as shown in Figs. 3 and 5 and Table 3. This feature is typical of an edge-dislocation array in a small-angle tilt GB. Second, the relatively wide extent of the local energy and local stress on both sides of the 5–3 unit in the Σ9

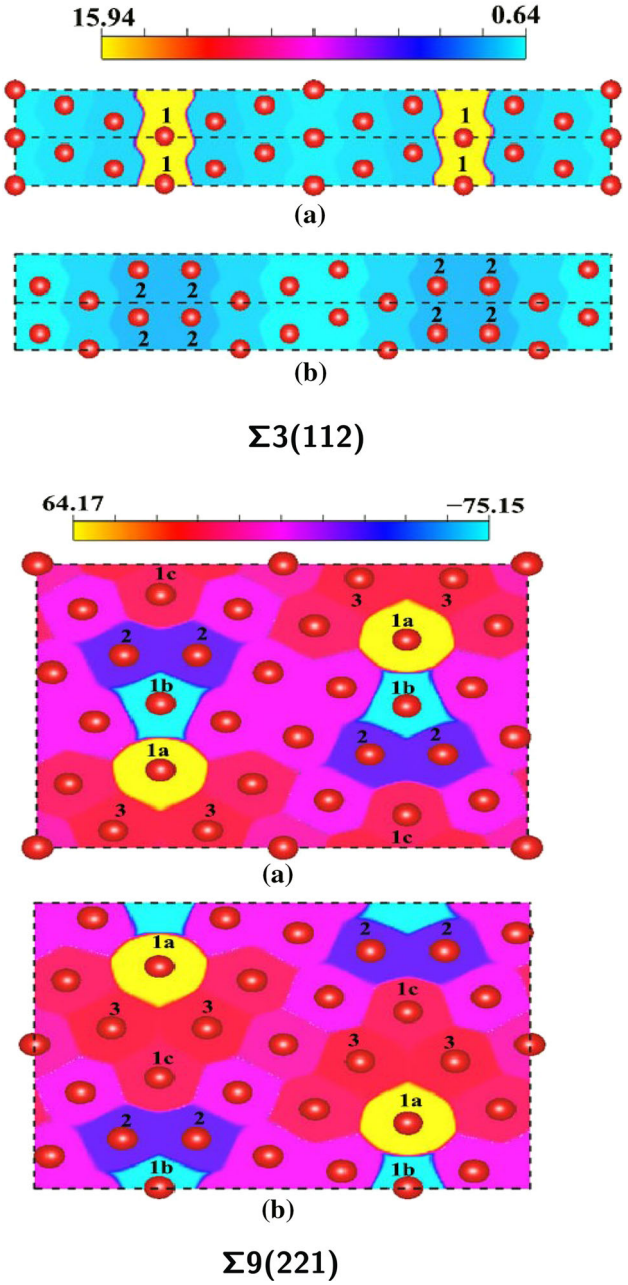

Fig. 5 (*Color online*) Plots of the atomic stress (*diagonal* sum) (in GPa) for the $\Sigma 3$ (112) and $\Sigma 9$ (221) GBs in Fe on the two (110) atomic planes of **a** $y = 0$ and **b** $y = |\mathbf{b}|/2$. *Different colors* represent different local stress values of each Bader region

(221) GB is also consistent with the view of the edge-dislocation array, in contrast to stable CSL GBs. Third, the energy increases and the magnitude of local stresses at the 5–3 unit are comparatively larger in the $\Sigma 9$ (221) GB. It can be said that the dislocation core in the bulk crystal or small-angle GBs has larger atomic energy increases and larger magnitudes of atomic stresses than the structural units in stable CSL GBs. For diamond STGBs with low rotation angles, these three aspects were also observed in the atomic energies and atomic stresses obtained by an empirical potential [8].

Local magnetic moment and local bonding nature

In our preceding work [11], we observed two kinds of interface atoms in the $\Sigma 3$ (111) and $\Sigma 11$ (332) GBs. One kind of interface atoms has larger atomic volumes or stretched bonds, while the other kind has shortened strong bonds with more covalent character. As mentioned above, the former kind of atoms have higher local energies and tensile stresses, while the latter kind of atoms have lower energies and compressive stresses. Furthermore, the former kind of atoms have enhanced magnetic moments due to the magnetovolume effect [14], and the latter kind of atoms have reduced magnetic moments due to increased occupancy in the minority-spin DOS via stronger *d*–*d* hybridization at shortened bonds. This kind of increased occupancy results in the minority-spin electron accumulation to such strengthened bonds.

Figure 6 shows the variation of the local magnetic moment compared to the local atomic volume in the $\Sigma 3$ (112) and $\Sigma 9$ GBs. Corresponding figures for the $\Sigma 3$ (111) and $\Sigma 11$ (332) GBs are given in [11]. Table 4 lists the magnetic moment of each interface atom, compared to its atomic volume and shorter bond lengths around it. The $\Sigma 9$ (221) GB reveals similar features to those of the $\Sigma 3$ (111) and $\Sigma 11$ (332) GBs [11], while the $\Sigma 3$ (112) GB reveals rather special features. In the $\Sigma 3$ (112) GB, the interface atom has the largest atomic volume, resulting in the largest increase in the magnetic moment due to the magnetovolume effect. The magnetic moment simply becomes the bulk value due to the recovery of the atomic volume inside the bulk regions. There are no compressed atomic volumes. The atomic volume change itself is rather small in this GB, resulting in the rather small increase in the magnetic moment even at the interface atom. Thus, the electronic structure change is not so remarkable in Fig. 7a. The minority-spin LDOS of the atom on layer "1" in the $\Sigma 3$ (112) GB shows minor reduction in the occupied portion and slight increase in the DOS at the Fermi level, resulting in a small increase in the magnetic moment as the magnetovolume effect.

For the $\Sigma 9$ (221) GB, however, very large (2.80 μ_B at "1a") and very small (1.77 μ_B at "1b") moments are observed as shown in Fig. 6 and Table 4. The magnetic moment at the atom of "1a" is the largest in the four GBs, which is consistent with the very large atomic volume (19 % expansion). The magnetic moment at the atom of "1b" is the lowest in the four GBs, which is also consistent with the very small atomic volume (7 % compression) and small bond lengths (2.22 Å). For the atoms of "1a" and on

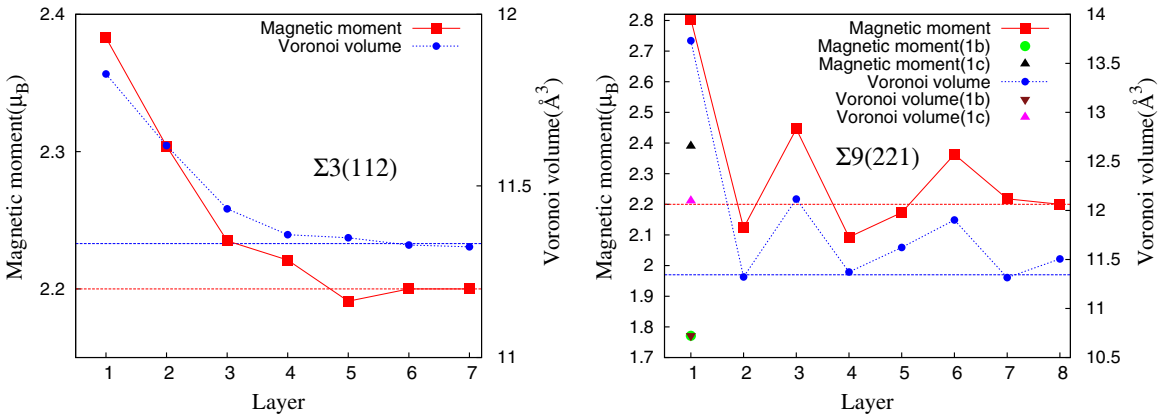

Fig. 6 (*Color online*) Variations of the local magnetic moments (in μ_B) and Voronoi volumes (in Å^3) in the atomic layers of the Σ3 (112) and Σ9 (221) GBs in Fe. The *red* and *blue horizontal broken lines* show the bulk magnetic moment (2.2 μ_B) and the bulk Voronoi volume (11.35 Å^3), respectively

Table 4 Local magnetic moments (in μ_B) and Voronoi volumes V_i against the bulk Voronoi volume V_0 for the interface atoms in the four STGBs in Fe

GB	Magnetic moment (μ_B)						V_i/V_0						Bond lengths (Å)				
Σ3 (112)	1	2	3				1	2	3				R_{12}	R_{13}	R_{22}	R_{23}	R_{24}
	2.38	2.30	2.24				1.05	1.03	1.01				2.52	2.48	2.44	2.44	2.44
Σ3 (111)	1	2	3	4			1	2	3	4			R_{22}	R_{25}	R_{23}		
	2.69	1.86	2.37	2.30			1.14	0.99	1.08	1.01			2.20	2.35	2.38		
Σ11 (332)	1a	1b	2	3	4		1a	1b	2	3	4		R_{22}	R_{1b4}	R_{26}	R_{24}	
	2.68	2.22	2.04	2.54	2.08		1.14	0.99	0.99	1.08	0.98		2.28	2.32	2.36	2.38	
Σ9 (221)	1a	1b	1c	2	3	4	1a	1b	1c	2	3	4	R_{1b4}	R_{22}	R_{25}	R_{1b2}	R_{27}
	2.80	1.77	2.39	2.12	2.45	2.09	1.19	0.93	1.05	0.99	1.05	1.01	2.22	2.33	2.34	2.34	2.39

Several short bond lengths in ascending order from the shortest in each GB [except for Σ3 (112) GB] are also listed. For the Σ3 (112) GB, the lengths of the first-neighbor bonds with larger deviations from the bulk length (2.45 Å) are listed in descending order

layers "2" and "3" the variations of the magnetic moments, combined with the atomic volume changes, are rather similar to the corresponding atoms in the Σ3 (111) and Σ11 (332) GBs. For the Σ9 (221) GB, there is a tendency that the variation in the magnetic moments extends rather deep inside the bulk regions due to the wide extent of the structural disorder.

About the LDOS's of the Σ9 GB in Fig. 7b, the atoms at "1a" and "1b" reveal the most remarkable changes in accordance with the largest deviations in the magnetic moments. As discussed in [11], the occupied portion in the minority-spin *d*-band DOS dominates the magnetic moment, because the majority-spin *d*-band DOS is almost fully occupied in any atoms. For the atom of "1a" due to the reduction of *d*–*d* hybridization by the larger atomic volume, the *d*-band width and the occupied portion in the minority-spin DOS are greatly reduced, resulting in the enhanced spin polarization. For the atom on layer "3" with an enhanced magnetic moment, similar features are observed in the LDOSs. For the atom of "1b" however, the enhanced *d*–*d* hybridization induces the increase in the occupied portion in the minority-spin DOS, resulting in the reduced spin polarization. There is an increased peak at about −2 eV in the minority-spin DOS of the atom "1b" which should be caused by the formation of strong bonds between the atom "1b" and the atoms on layer "4" and between the atom "1b" and the atoms on layer "2" as shown in Fig. 2. Similar increase of peaks in the minority-spin DOSs is observed in the atoms on layers "2" and "4" in Fig. 7b, which also lead to the reduced magnetic moments at these atoms.

In this way, for the Σ9 (221) GB, we can predict the accumulation of minority-spin electrons at the bonds between the atoms at "1b" and layer "4", between the atoms on layer "2" and between the atoms at "1b" and layer "2" due to the increased occupancies in the minority-spin LDOS's. Figure 8 clearly shows such minority-spin electron accumulation at these bonds, as observed in the Σ3

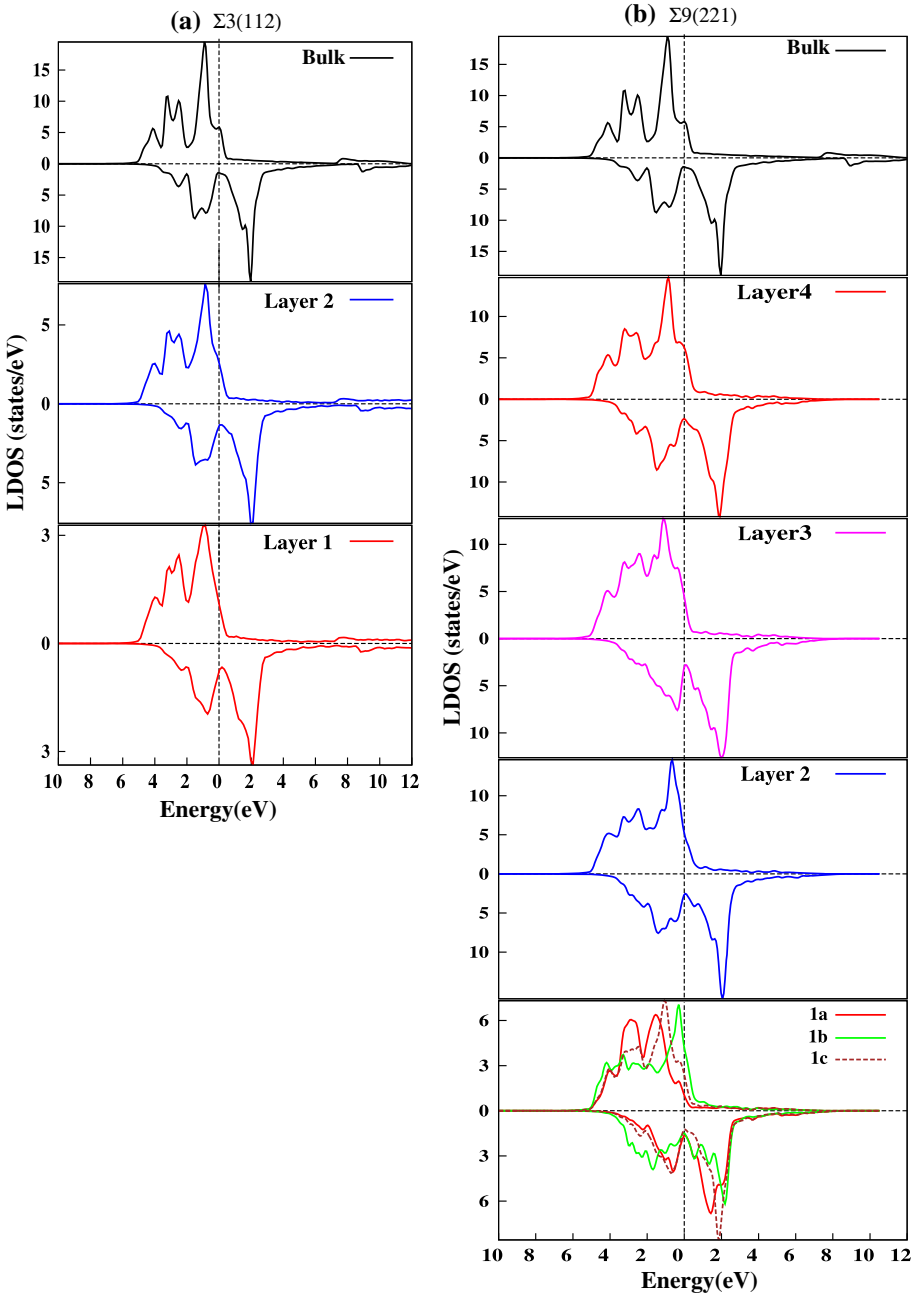

Fig. 7 (*Color online*) LDOSs for the *d* orbitals of the atomic layers at the interface regions in the Σ3 (112) (**a**) and Σ9 (221) (**b**) GBs of Fe. The Fermi level is set to be zero

(111) and Σ11 (332) GBs [11]. On the other hand, for the atoms with enhanced magnetic moments, there should occur the decrease in the minority-spin electron densities, which can be clearly seen around the atom of "1a" of the Σ9 (221) GB in Fig. 8. This feature is also seen around the atom on layer "1" in the Σ3 (112) GB in Fig. 8. For the present four STGBs, we can generally observe the apparent correlation among the local magnetic moments, the local structural features as atomic volumes and bond lengths, the LDOS features, and the minority-spin electron distribution.

Local Young's modulus

Figure 3 also shows the local Young's modulus of each atom in the GB supercell for the four kinds of ⟨110⟩ STGBs in bcc Fe. Table 5 lists the averaged Young's moduli for GB regions of various widths as well as cell-averaged Young's moduli of the GB and bulk supercells. Note that the bulk Young's moduli by the bulk supercells are substantially larger than previous theoretical and experimental values of bcc Fe [40] due to the present

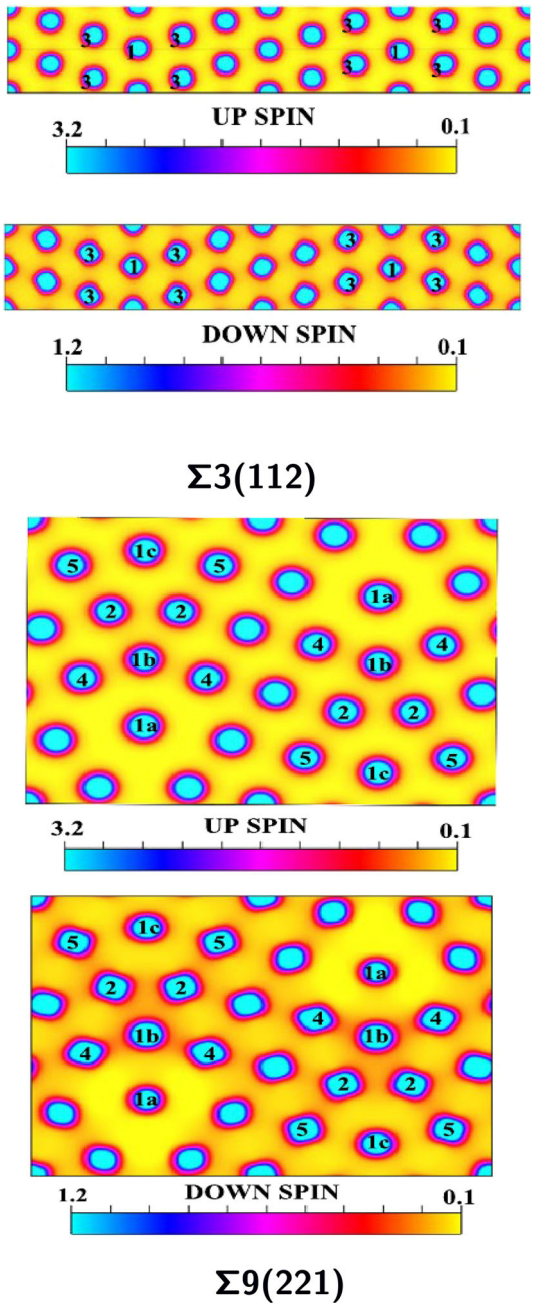

Fig. 8 (*Color online*) Two-dimensional plots of the charge densities of up-spin and down-spin electrons in the $\Sigma 3$ (112) (*upper two panels*) and $\Sigma 9$ (221) (*lower two panels*) GBs of Fe. For the $\Sigma 3$ (112) GB, the supercell is repeated along the z direction for a better view

condition of the fixed cell parameters normal to the tensile or compressive direction. This problem prevents direct quantitative comparison with experiments, while the present purpose is to examine the effect of interface configurations on the interface elastic or mechanical properties. We can observe the correlation between the local or averaged Young's moduli and the structural disorder or GB energies for the four GBs. For the Young's modulus averaged in the structural units (in the atoms until layer "4") in Table 5, the decrease against the bulk value obtained by the bulk supercell are 12 % (10 %), 31 % (27 %), 29 % (25 %), and 43 % (41 %) for the $\Sigma 3$ (112), $\Sigma 3$ (111), $\Sigma 11$ (332), and $\Sigma 9$ (221) GBs, respectively. The order of the decrease in the averaged Young's moduli for the four GBs is similar to the order of the GB energies. This is because the interface elastic property or averaged hardness of interface bonding is dominated by the status of the interfacial bonds or interfacial structural disorder, dominating the GB energy.

In Fig. 3, we can analyze the relation among the local Young's modulus, local configuration, local energy, and local stress. For the $\Sigma 3$ (112) GB, the presence of an interface consisting of four-membered rings leads to slight lowering of the Young's modulus at the interface. It is interesting that the slight lowering extends in a rather wide region. This is because the Voronoi volume to define the local strain is affected by the second neighbors in a bcc structure, and thus the presence of the interface affects the local Young's modulus in a wide extent. For the other three STGBs, the width of the lowering of the local Young's modulus has correlation with the width of the local energy increase and local stress variation, corresponding to the width of local structural disorder. Thus, the width of the lowering of the local Young's modulus increases in the order of the $\Sigma 3$ (111), $\Sigma 11$ (332), and $\Sigma 9$ (221) GBs as shown in Fig. 3. The depth of the lowering also has correlation with the degree of the local structural disorder, the local stress variation, and the local energy increase. The lowest local Young's modulus is located at the interface layer in each GB, and is 175.38, 195.79, and 129.94 GPa for the $\Sigma 3$ (111), $\Sigma 11$ (332), and $\Sigma 9$ (221) GBs, respectively. This is consistent with the point that the magnitudes of the local energy increase and local stress at the interface layers are larger in the $\Sigma 3$ (111) GB than in the $\Sigma 11$ (332) GB, and the largest in the $\Sigma 9$ (221) GB in Fig. 3. By the way, it is reasonable that the strongly compressed atoms as "1b" in the $\Sigma 11$ (332) and $\Sigma 9$ (221) GBs have lower local Young's moduli.

Concluding remarks

We have dealt with four kinds of $\langle 110 \rangle$ STGBs in bcc Fe, the $\Sigma 3$ (112), $\Sigma 3$ (111), $\Sigma 11$ (332), and $\Sigma 9$ (221) GBs with the rotation angles as $\theta = 109.47°$, 70.53°, 50.48°, and 38.94°, respectively. These four GBs can be regarded as representatives. The $\Sigma 3$ (112) GB consists of one kind of specially stable structural units, and can be classified into stacking-fault type. The $\Sigma 3$ (111) and $\Sigma 11$ (332) GBs can be classified into typical CSL GB type, consisting of ordered structural units. The $\Sigma 3$ (111) GB consists of only

Table 5 Averaged Young's moduli in the interface regions of the four STGBs in Fe

GB	Y_{GB}^{cell}	Y_{bulk}^{cell}	Y_{GB}^{SU}	Y_{GB}^{1-4}	Y_{GB}^{1-5}
Σ3 (112)	286.28	309.73	273.66 (0.88)	277.95 (0.90)	281.39 (0.91)
Σ3 (111)	242.83	317.25	218.72 (0.69)	229.92 (0.73)	242.25 (0.76)
Σ11 (332)	258.75	316.78	226.06 (0.71)	235.86 (0.75)	241.70 (0.76)
Σ9 (221)	210.93	303.73	172.71 (0.57)	178.97 (0.59)	192.39 (0.63)

Y_{GB}^{cell} and Y_{bulk}^{cell} are the cell-averaged Young's moduli for the GB and bulk supercells, respectively, obtained by Eq. (9). Y_{GB}^{SU}, Y_{GB}^{1-4} and Y_{GB}^{1-5} are the averaged local Young's moduli in the atoms of the structural units, until layer "4", and until layer "5", respectively. All the quantities are in GPa unit. Values in the parentheses are the ratio against the value of Y_{bulk}^{cell} for each GB

the 5–3 units, while the Σ11 (332) GB consists of one-by-one mixture of the 5–3 and bulk units. The Σ9 (221) GB consists of one-by-two mixture of the 5–3 and bulk units, while this has an aspect of a small-angle tilt GB, because the 5–3 unit between the bulk units can be regarded as a dislocation core introduced in the bulk crystal.

For the Σ3 (112) GB, the structural units consisting of four-membered rings have no coordination defects or substantial bond-length distortions, except for bond-angle disorder and small interlayer dilatation at the interface, leading to small atomic energy increases, and small atomic stresses, small magnetic moment increase, and small LDOS changes. Thus, this GB indeed has special stability as classified into staking fault or twin type, similar to the Σ3 (111) GB in fcc metals.

From the Σ3 (111) GB, consisting of only the 5–3 units, the mixing ratio of the bulk units increases for the Σ11 (332) and Σ9 (221) GBs. There is a tendency that the local energy and local stress at the 5–3 units are relaxed from the Σ3 (111) GB to the Σ11 (332) GB by the introduction of bulk units, while these are increased from the Σ11 (332) GB to the Σ9 (221) GB. The extent of the energy increase and stress variation on both sides of the interface, correlated with the structural distortions, is increased in the order of the Σ3 (111), Σ11 (332), and Σ9 (221) GBs. In the Σ9 (221) GB, tensile and compressive stresses are greatly enhanced at both the edges of the 5–3 unit, which is consistent with the view of an edge-dislocation array in a small-angle tilt GB, as well as the wider extent of the strain on both sides of the unit.

For the Σ9 (221) GB, we observed that there are two kinds of interface atoms similar to the Σ3 (111) and Σ11 (332) GBs found in our preceding work [11]. Interface atoms with larger atomic volumes or stretched bonds show higher local energy increases and tensile stresses with enhanced magnetic moments via reduced occupied portion in the minority-spin LDOS due to reduced *d–d* hybridization. On the other hand, interface atoms with shortened bonds or reduced atomic volumes show relatively smaller energy increases and compressive stresses with reduced magnetic moments via increased occupied portion in the minority-spin LDOS due to enhanced *d–d* hybridization at shortened bonds, resulting in minority-spin electron accumulation in such bonds. These features should be common in GBs or defects in bcc Fe.

The local Young's moduli averaged in the structural units for the four GBs range from 60 to 90 % of the bulk Young's modulus in accordance with the GB energies. The width and degree of lowering of local Young's modulus at interface regions in each GB coincide with the width and degree of structural disorder. The local Young's modulus has clear correlation with the local energy increase and the magnitude of local stresses in each GB. The current examination, the first of its kind, has shown that the local Young's modulus is an effective tool in understanding the local elastic properties when it is combined with the local energy and local stress analysis.

Finally, the ab initio results such as boundary energies and stable configurations may depend on the size of the supercells. It is desirable to select supercells with enough thick bulk regions between the interfaces, but the practical judgement of this is rather difficult and we have to deal with relatively smaller supercells. Importantly, our local energy and local stress schemes provide useful information on the necessary and sufficient thickness of the bulk region. The local energy increase and local stress at the central part of the bulk region should be negligible, which is the necessary condition. From this point of view, the size of the supercell of the Σ9 GB may not be enough. However, we would like to reiterate that the effects of local structural disorder around the structural units can be effectively analyzed by the local energy and local stress schemes even if the cell size is not enough.

Acknowledgements The present study was supported by JST Industry-Academia Collaborative Programs, "Materials Strength from Hamiltonian". The development of computational techniques for the local energy and local stress analysis was supported by the Grand-in-Aid for Scientific Research (KAKENHI 23710107) and the Grand-in-Aid for Scientific Research on Innovative Areas, "Bulk Nanostructured Metals" and partially supported by the Elements Strategy Initiative for Structural Materials (ESISM) through MEXT, Japan. The authors thank Professor T. Mohri and Dr. S. Ishibashi for fruitful discussions.

References

1. Sutton AP, Balluffi RW (1995) Interfaces in crystalline materials. Clarendon Press, Oxford
2. Priester L (eds) (2011) Grain boundaries and crystalline plasticity. Wiley-ISTE, London
3. Sutton AP, Vitek V (1983a) On the structure of tilt grain boundaries in cubic metals. I. Symmetrical tilt boundaries. Philos Trans R Soc 309:1–36
4. Sutton AP, Vitek V (1983b) On the structure of tilt grain boundaries in cubic metals. II. Asymmetrical tilt boundaries. Philos Trans R Soc Lond A 309:37–54
5. Sutton AP, Vitek V (1983c) On the structure of tilt grain boundaries in cubic metals. III. Generalizations of the structural study and implications for the properties of grain boundaries. Philos Trans R Soc Lond A 309:55–68
6. Sutton AP, Balluffi RW (1990) Rules for combining structural units of grain boundaries. Philos Mag Lett 61:91–94
7. Nakashima H, Takeuchi M (2000) Grain boundary energy and structure of α-Fe ⟨110⟩ symmetric tilt boundary. ISIJ 86:357–362
8. Shenderova OA, Brenner DW, Yang LH (1999) Atomistic simulations of structures and mechanical properties of polycrystalline diamond: symmetrical ⟨001⟩ grain boundaries. Phys Rev B 60:7043–7052
9. Kohyama M (2002) Computational studies of grain boundaries in covalent materials. Model Simul Mater Sci Eng 10:R31–R51
10. Read WT, Shockley W (1950) Dislocation models of crystal grain boundaries. Phys Rev 78:275–289
11. Bhattacharya SK, Tanaka S, Shiihara Y, Kohyama M (2013) Ab initio study of symmetrical tilt grain boundaries in bcc Fe: structural units, magnetic moments, interfacial bonding, local energy and local stress. J Phys Condens Matter 25(13):135004-1–135004-14
12. Ogata S, Umeno Y, Kohyama M (2009) First-principles approaches to intrinsic strength and deformation of materials: perfect crystals, nano-structures, surfaces and interfaces. Model Simul Mater Sci Eng 17:013001-1–013001-33
13. Yesilleten D, Nastar M , Arias TA , Paxton AT, Yip S (1998) Stabilizing role of itinerant ferromagnetism in intergranular cohesion in iron. Phys Rev Lett 81:2998–3001
14. Čák M, Šob M, Hafner J (2008) First-principles study of magnetism at grain boundaries in iron and nickel. Phys Rev B 78:054418-1–054418-10
15. Wachowicz E, Ossowski T, Kiejna A (2010) Cohesive and magnetic properties of grain boundaries in bcc Fe with Cr additions. Phys Rev B 81:094104-1–094104-9
16. Du YA, Ismer L, Rogal J, Hickel T, Neugebauer J, Drautz R (2011) First-principles study on the interaction of H interstitials with grain boundaries in α- and γ-Fe. Phys Rev B 84:144121-1–144121-13
17. Shiihara Y, Kohyama M, Ishibashi S (2010) Ab initio local stress and its application to Al(111) surfaces. Phys Rev B 81:075441-1–075441-11
18. Shibuta Y, Takamoto S, Suzuki T (2009) Dependence of the grain boundary energy on the alloy composition in the bcc iron chromium alloy: a molecular dynamics study. Comput Mater Sci 44:1025–1029
19. Shibuta Y, Takamoto S, Suzuki T (2008) A molecular dynamics study of the energy and structure of the symmetric tilt boundary of iron. ISIJ Int 48:1582–1591
20. Terentyev D, He X, Serra A, Kuriplach J (2010) Structure and strength of ⟨110⟩ tilt grain boundaries in bcc Fe: an atomistic study. Comput Mater Sci 49:419–429
21. Yu M, Trinkle DR (2011) Accurate and efficient algorithm for Bader charge integration. J Chem Phys 134:064111-1–064111-8
22. Wang H, Kohyama M, Tanaka S, Shiihara Y (2013) Ab initio local energy and local stress: application to tilt and twist grain boundaries in Cu and Al. J Phys Condens Matter 25:305006-1–305006-13
23. Blöchl PE (1994) Projector augmented-wave method. Phys Rev B 50:17953–17979
24. Kresse G, Joubert D (1999) From ultrasoft pseudopotentials to the projector augmented-wave method. Phys Rev B 59:1758–1775
25. Perdew JP, Burke K, Ernzerhof M (1996) Generalized gradient approximation made simple. Phys Rev Lett 77:3865–3868
26. Monkhorst HJ, Pack JD (1976) Special points for Brillouin-zone integrations. Phys Rev B 13:5188–5192
27. Kresse G, Furthmüller J (1996) Efficiency of ab-initio total energy calculations for metals and semiconductors using a plane-wave basis set. Comput Mater Sci 6:15–50
28. Kresse G, Furthmüller J (1996) Efficient iterative schemes for ab initio total-energy calculations using a plane-wave basis set. Phys Rev B 54:11169–11189
29. Ishibashi S, Tamura T, Tanaka S, Kohyama M, Terakura K (2007) Ab initio calculations of electric-field-induced stress profiles for diamond/c-BN(110) superlattices. Phys Rev B 76:153310-1–153310-4
30. Chetty N, Martin RM (1992) First-principles energy density and its applications to selected polar surfaces. Phys Rev B 45:6074—6088
31. Filippetti A, Fiorentini V (2000) Theory and applications of the stress density. Phys Rev B 61:8433–8442
32. Bader RF (1990) Atoms in molecules: a quantum theory. Oxford University Press, Oxford
33. Yu M, Trinkle DR, Martin RM (2011) Energy density in density functional theory: application to crystalline defects and surfaces. Phys Rev B 83:115113-1–115113-10
34. Nielsen OH, Martin RM (1985) Quantum-mechanical theory of stress and force. Phys Rev B 32:3780–3791
35. Ziesche P, Gräfenstein J, Nielsen OH (1988) Quantum-mechanical stress and a generalized virial theorem for clusters and solids. Phys Rev B 37:8167–8178
36. Godfrey MJ (1988) Stress field in quantum systems. Phys Rev B 37:10176–10183
37. Rogers CL, Rappe AM (2002) Geometric formulation of quantum stress fields. Phys Rev B 65:224117-1–224117-8
38. Becke AD (1988) A multicenter numerical integration scheme for polyatomic molecules. J Chem Phys 88:2547–2553
39. Gao N, Fu C-C, Samaras M, Schäublin R, Victoria M, Hoffelner W (2009) Multiscale modelling of bi-crystal grain boundaries in bcc iron. J Nucl Mater 385:262–267
40. Zhang H, Johansson B, Vitos L (2009) Ab initio calculations of elastic properties of bcc Fe–Mg and Fe–Cr random alloys. Phys Rev B 79:224201-1–224201-10